The 2010 Russian drought impact on satellite measurements of solar-induced chlorophyll fluorescence: Insights from modeling and comparisons with the Normalized Differential Vegetation Index (NDVI)

Y. Yoshida[a,b], J. Joiner[a], C. Tucker[a], J. Berry[c], J.-E. Lee[d], G. Walker[b], R. Reichle[a], R. Koster[a], A. Lyapustin[a], and Y. Wang[e]

[a]NASA Goddard Space Flight Center, Greenbelt, MD, USA
[b]Science Systems and Applications, Inc., Lanham, MD, USA
[c]Carnegie Institution for Science, Stanford, CA, USA
[d]Brown University, Providence, RI, USA
[e]Joint Center for Environment Technology, University of Maryland, Baltimore County, MD, USA

*Corresponding author: Yasuko Yoshida, Code 614 NASA Goddard Space Flight Center, Greenbelt, MD 20771, USA. Email: yasuko.yoshida-1@nasa.gov. Phone: 1-301-614-6009; Fax: 1-301-614-5903.

Keywords: vegetation, drought, chlorophyll, vegetation index, NDVI, MODIS, fluorescence, GOME-2, APAR, FPAR, gross primary productivity

Abstract

We examine satellite-based measurements of chlorophyll solar-induced fluorescence (SIF) over the region impacted by the Russian drought and heat wave of

2010. Like the popular Normalized Difference Vegetation Index (NDVI) that has been used for decades to measure photosynthetic capacity, SIF measurements are sensitive to the fraction of absorbed photosynthetically-active radiation (fPAR). However, in addition, SIF is sensitive to the fluorescence yield that is related to the photosynthetic yield. Both SIF and NDVI from satellite data show drought-related declines early in the growing season in 2010 as compared to other years between 2007 and 2013 for areas dominated by crops and grasslands. This suggests an early manifestation of the dry conditions on fPAR. We also simulated SIF using a global land surface model driven by observation-based meteorological fields. The model provides a reasonable simulation of the drought and heat impacts on SIF in terms of the timing and spatial extents of anomalies, but there are some differences between modeled and observed SIF. The model may potentially be improved through data assimilation or parameter estimation using satellite observations of SIF (as well as NDVI). The model simulations also offer the opportunity to examine separately the different components of the SIF signal and relationships with Gross Primary Productivity (GPP).

1. Introduction

For over 30 years, the primary tool for monitoring vegetation globally from space has been reflectance measurements at visible and near-infrared wavelengths (*e.g.*, Tucker, 1979; Myneni *et al*., 1997). Since 1981, there is a continuous record of the Normalized Difference Vegetation Index (NDVI) from the Advanced Very High Resolution Radiometer (AVHRR) series of instruments on meteorological satellites (Tucker *et al*., 2005). The NDVI and similar indices utilize visible and near-infrared reflectances on both sides of the so-called red-edge (their difference normalized by their sum) and are sensitive to the amount of green biomass within a satellite pixel. These indices and related parameters have been widely used to examine spatial and inter-annual variations in vegetation and for many other applications including estimation of gross primary productivity (GPP) (*e.g.*, Tucker & Sellers, 1986; Randerson *et al.*, 1997; Running *et al.*, 2004).

Satellite measurement of solar-induced fluorescence (SIF) from chlorophyll has emerged over the last few years as a different method to monitor vegetation globally from space (*e.g.,* Guanter *et al.*, 2007, 2012; Joiner *et al.*, 2011, 2012; Frankenberg *et al.,* 2011). SIF measurements are based on the fact that a small fraction of the energy absorbed by vegetation (of the order of a percent) is emitted as fluorescence. The fluorescent emission has two peaks near 685 and 740 nm, known as the red and far-red emission features. All of the satellite measurements reported thus far have been in the far-red spectral region, where reabsorption of the fluorescence within the leaves and canopy is relatively small.

Relationships between SIF, NDVI, GPP and other parameters can be understood within the context of the light-use efficiency (LUE) model (Monteith, 1972), *i.e.*,

$$\mathrm{GPP} = \mathrm{LUE} * \mathrm{fPAR} * \mathrm{PAR} = \mathrm{LUE} * \mathrm{APAR}, \quad (1)$$

where fPAR is the fraction of absorbed Photosynthetically-Active Radiation, and APAR=fPAR*PAR is the total amount of absorbed PAR. The amount of SIF at the top-of-canopy can be approximated in a similar form, *i.e.,*

$$\mathrm{SIF} = \Theta_f * \mathrm{fPAR} * \mathrm{PAR} * \Omega_c = \Theta_f * \mathrm{APAR} * \Omega_c, \quad (2)$$

where Θ_f is the fluorescence yield at the membrane scale, and Ω_c is a radiative transfer function linking the escape of fluorescence from the top of canopy to the emission of fluorescence at the scale of the chloroplast membranes. It is reasonable to assume that Ω_c remains fairly constant for repeat observations of a vegetated area made from a satellite over a limited period of time when vegetation structure is not changing.

The NDVI is an indicator of potential photosynthesis or photosynthetic capacity as it is a measure of chlorophyll abundance and energy absorption that varies with abiotic conditions (Myneni *et al*., 1995). SIF responds linearly to changes in APAR, but this will be convolved with changes in Θ_f that may also be related to stress. NDVI also responds to stress by a reduction of energy absorption, and this occurs on the order of a few days (Tucker *et al*., 1981).

If Ω_c is assumed constant, and the ratio LUE to Θ_f also remains constant, then it can be seen from Eqs. (1) and (2) that SIF will be linearly related to GPP. Theory and measurements suggest that under strong illumination, such as natural illumination present during daytime satellite overpasses, the ratio of LUE to Θ_f remains relatively constant, at least for fluorescence from photosystem II (e.g., Berry *et al.*, 2013; Porcar-Castell *et al*., 2014). Previous studies have focused on relationships between GPP estimated from flux tower measurements and satellite-based SIF in terms of both in terms of magnitude (Guanter *et al*., 2014) and seasonal variations (Joiner *et al*., 2014). These studies have demonstrated that on a weekly to monthly time-scale, there is a high correlation between GPP and SIF.

Other studies have examined relationships between remotely-sensed SIF and LUE including stress. These studies have utilized ground-based measurements (*e.g.*, Louis *et al*., 2005; Meroni *et al*., 2008; Middleton *et al*., 2009, 2011; Damm *et al*., 2010; Daumard *et al*., 2010) as well as satellite-based SIF (*e.g.*, Lee *et al*., 2013; Parazoo *et al*., 2013;

Zhang *et al*., 2014). The latter studies with satellite data have focused primarily on the Amazonia basin and maize and soybean croplands in the midwest US. Some of these studies show that stress, including heat and moisture stress, can manifest itself earlier or be more pronounced in SIF as compared with vegetation indices (*e.g*., Daumard *et al*., 2010). This can occur when there is a decrease in the Θ_f component of SIF rather than, or in addition to, a decrease in fPAR that would be reflected in both SIF and NDVI.

In this work, we examine the relative importance of Θ_f and fPAR to the SIF signal in a situation of high stress: the regional drought and heat wave that occurred in western Russia due to a persistent blocking ridge over central Europe during the months June through August 2010 (*e.g.,* Grumm, 2011). Societal impacts of this event included massive peat and forest fires, a decrease in wheat production of 20-30% relative to 2009, and an increase in death rates in nearby cities including Moscow. Because this drought and heat wave occurred over an extensive region, we can examine its effects on SIF and NDVI over areas covered with predominantly different vegetation types. This allows for an assessment of whether certain vegetation types are more or less prone to stress and damage and whether stress is observed earlier in the SIF data for different vegetation types.

In addition to examining satellite data, we simulate SIF and other parameters using a global land surface model forced by observation-based meteorological fields. Within this simulation, we are able to examine the effects of the drought and heat wave on fPAR and photosynthesis. This provides further insight into the relative effects of the drought on LUE, Θ_f, PAR, and fPAR and demonstrates the skill of the model in predicting drought-induced anomalies. To our knowledge, this region has not yet been examined in detail in the literature with respect to satellite-based SIF observations.

2. Data and methods

We examine data within six regions of size 2° longitude by 1° latitude over western Russia in areas impacted by the drought and heat wave in 2010. Because the SIF signal has a lower signal to noise ratio as compared with the NDVI, we need to compute averages over spatial domains approximately this size. The individual regions were chosen because they contain various fractions of different vegetation types as shown in Figure 1. The location of each box and dominant International Geosphere Biosphere Programme (IGBP) vegetation type from the MODIS Land Cover Type Climate Modeling Grid (CMG) product for 2010 are listed in Table 1 (Friedl *et al*., 2010). We compute 8-day averages of various meteorological and satellite vegetation parameters throughout the growing season separately for 2010 (the drought year) and for all other years with available satellite GOME-2 SIF data (2007 to 2013 excluding 2010, hereafter referred to as the climatology).

2.1 GOME-2 SIF

The approach to retrieve the SIF signal from space was first demonstrated by observing the filling-in of the strong oxygen A-band absorption feature (Guanter *et al*., 2007). As this approach is difficult to implement globally, subsequent satellite retrievals utilized the filling-in of solar Fraunhofer lines surrounding the oxygen A-band (near 758 and 770 nm) using high spectral resolution measurements from a Fourier transform spectrometer on the Japanese Greenhouse gases Observing SATellite (GOSAT) (Joiner *et al*., 2011, 2012; Frankenberg *et al*., 2011; Guanter *et al*., 2012). Later it was shown that

SIF could be retrieved at 866 nm using hyperspectral measurements from the SCanning Imaging Absorption spectroMeter for Atmospheric CHartographY (SCIAMACHY) on board the European Space Agency's ENVIronmental SATellite (ENVISAT) (Joiner *et al*., 2012) and near 740 nm with the Global Ozone Monitoring Instrument 2 (GOME-2) on MetOp satellites (Joiner *et al*., 2013, 2014). While spatial and temporal variations in SIF from GOSAT and GOME-2 are comparable, GOME-2 SIF has better temporal and spatial coverage than GOSAT owing to greater sampling. We therefore use GOME-2 SIF exclusively for this study. The MetOp satellites, like ENVISAT and GOSAT, are in sun-synchronous orbits. The MetOp local overpass times are ~09:30.

GOME-2 is a grating spectrometer that measures backscattered sunlight in a scanning nadir-viewing geometry at wavelengths between 270 and 800 nm (Munro *et al*., 2006). GOME-2 instruments have been launched on the European Meteorological Satellites (EUMETSAT) MetOp A and B platforms on 19 October 2006 and 17 September 2012, respectively. Here, we use data from MetOp A covering the period 2007-2013. The nominal ground pixel lengths near nadir are approximately 40 km and 80 km in the along- and across-track directions, respectively, with a swath of width 1920 km. GOME-2 achieves global coverage in this configuration within about 1.5 days. Since 15 July 2013, the GOME-2 instruments onboard MetOp A and B operate in a tandem mode. In this mode, GOME-2 onboard MetOp B makes measurements with the nominal swath width and pixel size, while GOME-2 onboard MetOp A measures in a reduced swath of 960 km and pixel size of ~40 km by 40 km.

GOME-2 SIF retrievals are derived for a particular viewing geometry in radiance units ($mW/m^2/nm/sr$) from the filling-in of solar Fraunhofer lines in the vicinity of the

740 nm far-red chlorophyll fluorescence emission peak similar to Joiner *et al*. (2013, 2014). The retrieval uses a principal component analysis approach with a simplified radiative transfer model to estimate atmospheric absorption, surface reflectance (varying with wavelength), and fluorescence emission. We have made several adjustments in the version 2.6 (v2.6) data set used here as compared with the approaches described Joiner *et al*. (2013, 2014); this reduces small biases that were present in previous versions. In v2.6 we use a reduced spectral fitting window between 734 and 758 nm with a single set of principal components (PCs) derived from cloudy data over ocean, desert, and ice/snow cover to estimate the spectral structure of atmospheric water vapor absorption and instrumental artifacts. We correct for drift in the absolute instrument calibration using GOME-2 solar spectra. Finally, we apply an *a posteriori* correction for small biases caused presumably by straylight and dark current as discussed in Köhler *et al*. (2014) using data over ocean. The GOME-2 v2.6 SIF data are publicly available from http://avdc.gsfc.nasa.gov.

We use v2.6 level 2 SIF retrievals in this study (pixel data as opposed to level 3 gridded data sets). For the time-series analysis, we average the GOME-2 data over a particular area in 8-day bins. Uncertainties are estimated in each 8-day bin as the root sum square of the standard error of the mean. A nominal constant error of 0.15 $mW/m^2/nm/sr$ was used to account for additional errors following Joiner *et al*. (2014). Unlike the NDVI, SIF is sensitive to the amount of solar irradiance at the surface (equation 2). When comparing directly with NDVI, we therefore normalize SIF by cosine of solar zenith angle, a proxy for the seasonal cycle of potential surface solar irradiance, and for the Sun-Earth distance.

2.2 MODIS NDVI

We examine three different NDVI data sets from the MODerate-resolution Imaging Spectroradiometer (MODIS) on the NASA Earth Observing System (EOS) Aqua satellite: 1) the standard MYD13Q1 vegetation indices data set (Huete *et al*., 2002); 2) the Global Inventory Modeling and Mapping Studies GIMMS NDVI data applied to Aqua MODIS (Tucker *et al*., 2005); 3) MODIS NDVI computed from surface reflectances from the Multi-Angle Implementation of Atmospheric Correction (MAIAC) algorithm (Lyapustin *et al*., 2011a,b). We focus on the Aqua GIMMS NDVI in the main text and show comparable results with the other NDVI data sets in the appendix. The Aqua satellite has an ascending node equator crossing near 13:30 LT. We estimate errors as sum of the standard error of the mean and a nominal empirically estimated constant error of 0.03.

2.3 MERRA reanalysis data

We examine several meteorological fields from the NASA Global Modeling and Assimilation Office (GMAO) Goddard Earth Observing System Data Assimilation System version 5 (GEOS-5) Modern-Era Retrospective Analysis for Research and Applications (MERRA) data set (Rienecker *et al*., 2011). These include surface skin temperatures (T_{skin}) and total profile soil wetness (soil moisture), which are from the Incremental Analysis Updates 2D simulated land surface diagnostics product. We also use temperature at 2 m above the displacement height and 2 m specific humidity from the IAU 2D atmospheric single-level diagnostics product to calculate vapor pressure deficit (VPD, the difference between the actual and saturation-vapor pressure). Here, we use daily-averaged fields generated at 2/3° longitude by 1/2° latitude resolution. Near-surface specific humidity anomalies (Fig. 2a) in July show significantly drier than average conditions (13-32%) over a large part of the area examined. The T_{skin} anomalies show that the heat wave (up to ~7K above normal for the monthly average) was confined to a smaller area in the western part of the region (Fig. 2b). Figure 2c indicates that VPD anomalies are heavily controlled by temperature; the VPD anomalies in August are smaller than those in July. Soil moisture for both months shows negative anomalies for all six boxes (Fig. 2d).

2.4 Catchment-CN land surface model simulations

We examine several variables obtained from an off-line run of the Catchment-CN land surface model (Koster *et al*., 2014). The Catchment-CN land surface model is essentially a merger of the energy and water budget framework of the NASA Global Modeling and Assimilation Office's Catchment model (Koster *et al*., 2000) with the prognostic carbon elements (and thus prognostic phenology elements) of the National Center for Atmospheric Research/Department of Energy (NCAR/DOE) Community Land Model 4 (CLM4) dynamic vegetation model (Thornton *et al*., 2009; Oleson *et al*., 2010). The merged Catchment-CN model has some unique features, including the ability to represent multiple vegetation regimes within a surface element, each static vegetation regime associated with a different dynamic hydrological regime. The fractional areas occupied by individual plant functional types in the merged system do not change, but vegetation growth, soil heterotrophic activity, carbon stocks, and other ecosystem states (such as those associated with leaf area index) vary prognostically. Comparison of simulated fPAR with satellite-based estimates from the GIMMS AVHRR dataset (Tucker *et al*., 2005) demonstrate that the model, while biased, captures well the controls imposed by water supply on the global distributions of phenological variables (Koster *et al*. 2014); overall, Catchment-CN is found to be a useful tool for the analysis of the connections between climate and vegetation.

Fluorescence was added to the model by including the approach detailed for a similar implementation within the CLM4 (Lee *et al.,* 2014). The fluorescence code uses as inputs the photosynthesis rate, the intracellular leaf CO_2, and the CO_2 compensation point; it produces as an output SIF, as a daily mean for both the sunlit and shaded portions of the canopy. We used a model calibrated to leaf scale measurements of chlorophyll fluorescence from pulse amplitude modulated (PAM) fluorometry to simulate Θ_f as a function of the rate of photosynthesis simulated within the model. Key model variables are the flux of absorbed PAR, the rate of photosynthetic electron transport provided by the photosynthesis parameterization, and the level of non-photochemical quenching that can be measured with PAM fluorometry.

The offline Catchment-CN simulations are driven with atmospheric forcing from the MERRA-Land reanalysis product (Reichle *et al*., 2011), which is identical to that of MERRA except that surface precipitation is corrected to a global, daily, 0.5^{o} gauge product. Full Catchment-CN model spin-up was ensured by cycling over a 35 year period several times prior to producing the simulation data examined here. The Catchment-CN model was run on 64,770 irregularly shaped tiles (or computational elements) based on watershed delineations with a mean area of 2,010 km^2 and median area of 1,186 km^2. We use monthly mean output generated at 2.5° longitude by 2.0° latitude resolution from 2007 to 2013 for all parameters examined including surface skin temperature, fPAR (calculated as APAR/PAR), PAR, SIF, and GPP.

3. Results

3.1 Seasonal anomalies

The top half of each of the six panels of Figure 3 (one panel for each of the box regions in Fig.1) shows the climatological seasonal cycles of GOME-2 SIF and GIMMS NDVI as well as the values of 2010 for April to September. The bottom half of each panel shows the 2010 anomalies of VPD and soil moisture from MERRA. We next discuss results for boxes grouped by dominant vegetation types.

3.1.1. Croplands

For the boxes dominated by croplands (1, 2, and 5), climatological SIF and NDVI reach their maxima in middle June to late July depending on location; croplands towards the east generally peak later. As has been shown in other studies for croplands (as well as mixed forest), SIF starts to decline earlier in autumn as compared with reflectance-based indices such as the NDVI; the earlier decline of SIF is in better agreement with GPP from flux tower measurements (Joiner *et al*., 2014). Soil moisture anomalies indicate substantially drier than normal conditions starting around the middle of May for these boxes. VPD anomalies are large for box 1 that is within the area impacted by the heat wave. Similar to the surface temperatures, VPD anomalies peak in late July. The SIF and NDVI 2010 negative anomalies in these boxes are significant. For box 1, within the heat wave region, there is a somewhat later and smaller 2010 anomaly as compared with the other two cropland-dominated boxes. This could be because box 1 is in the basin of the Volga river that supplies ground water. Both SIF and NDVI indicate a slight partial recovery in August in boxes 1 and 2 only. There is a very strong correspondence between the GIMMS NDVI and SIF for all areas.

3.1.2. Grasslands and mixed forest

Boxes 3, 4, and 6 are primarily covered by grasslands and mixed forest. Box 3, composed primarily of mixed forest, appears to be less affected by drought than the other regions examined; the differences between the climatology and 2010 for SIF and NDVI are not statistically significant. Box 4, which is primarily grasslands, shows negative 2010 anomalies for both NDVI and SIF starting in early June. In contrast, box 6, which contains a mixture of grasslands and mixed forests, shows only small negative 2010 anomalies starting in late June.

3.2 Land surface modeling results

Figure 4 shows monthly means of the Catchment-CN land surface model output for the climatology and for 2010 in the six boxes. Parameters examined are fPAR, PAR APAR, and LUE. In Figure 5, SIF and GPP as well as SIF and GPP normalized with respect to incoming PAR are shown. Surface skin temperature and soil moisture (root zone) are shown in Figure 6. There are significant negative 2010 anomalies in GPP for all boxes starting mostly in June, which are influenced by negative anomalies in LUE. The surface skin temperatures are generally higher in 2010 for all regions as may be expected in conjunction with lower GPP. Soil moisture shows clear negative 2010 anomalies after May-April in the most of boxes except boxes 1 and 3, where there are negative anomalies for the 2010 growing season.

In contrast, the model's fPAR does not show a 2010 anomaly for box 3 dominated by mixed forest. In addition, the model's fPAR negative anomalies for the other boxes generally begin in July or August, about one month later than the GPP anomalies. PAR 2010 anomalies, on the other hand, are generally insignificant to positive, owing to decreases in cloudiness during the peak drought months. Because the model's 2010 PAR and fPAR anomalies are of opposite sign, this leads to smaller negative or insignificant 2010 APAR anomalies as compared with fPAR anomalies.

The model's 2010 SIF anomalies are somewhat smaller (in a percentage sense) than those of GPP. For example, when GPP drops to near zero starting in August for box 5, while the simulated SIF remains slightly above zero for August 2010. The model's 2010 SIF anomalies in most boxes are significant starting in July, while GPP negative anomalies begin in June for all boxes. However, when normalized with respect to incoming PAR, SIF shows earlier negative anomalies (starting in June) for most boxes and significant anomalies for all boxes, which is similar to the GOME-2 SIF anomalies. However, the model's 2010 negative fPAR anomalies start later (July), while the GIMMS NDVI anomalies begin earlier similar to the SIF anomalies. This indicates that the model's fPAR response to drought/heat stress may have occurred somewhat late.

In our analysis of GOME-2 SIF in Fig. 3, we partially filtered for clouds; we removed pixels with effective cloud fractions > 0.15. We also normalize SIF with respect to the incoming clear-sky PAR. It should be noted that the spectral signature of SIF is not affected by clouds. The main effect of clouds on satellite-observed SIF is a shielding effect that reduces the amount of canopy-level SIF that is observed by the satellite instrument. The cloud-shielding effect is relatively small for thin and broken clouds with low cloud fractions. For example, Frankenberg *et al.* (2013) showed with simulated data that 20% or less of the canopy-level SIF signal is lost from satellite observation for cloud optical thicknesses up to 5. To be consistent, because the PAR-normalized, cloud-filtered GOME-2 SIF is biased toward clear skies, it should be compared with the PAR-normalized SIF from the model.

The model produces similar (PAR-normalized) SIF anomalies as compared with the GOME-2 data, although the overall phenology is somewhat different. One difference between model and GOME-2 SIF is for the mixed forest dominated box 3. For this box, GOME-2 SIF does not show a significant 2010 SIF negative anomaly, while the model simulates a significant (normalized) anomaly. The fact that NDVI does not show a significant 2010 anomaly for this box is consistent with the absence of an fPAR anomaly in the model. Therefore, the model's negative 2010 photosynthesis anomaly may be overestimated for this box.

To provide an overall regional context, Figure 7 shows maps of 2010 anomalies of fPAR, PAR, APAR, and LUE from the land-surface model for July and August. fPAR anomalies are smaller in July as compared with August. The higher positive 2010 PAR anomalies in July are reflected in the APAR anomalies and lead to some positive anomalies in APAR. LUE anomalies are negative over most of the domain and more significant in August.

Figure 8 also shows maps of 2010 anomalies from the land-surface model for SIF, GPP, and both quantities normalized with respect to PAR. As noted above, the positive anomalies in GPP and SIF in the northwestern portion of the study area result from PAR anomalies, while the negative anomalies towards the south in the PAR-adjusted quantities are shown with contributions from fPAR; the increase in magnitude of the negative anomalies from July to August results primarily from the decline in fPAR over that period.

Figure 9 compares the model's SIF with that from GOME-2 for both the climatology and 2010 anomalies. Here, the model SIF is normalized with respect to PAR and GOME-2 SIF is scaled as before by cosine of the solar zenith angle. The satellite SIF data are shown at both the model resolution and a higher spatial resolution. To provide more samples per gridbox, we retain all data with effective cloud fractions up to 0.3. This did not substantially change the spatial or temporal SIF distributions as compared with a lower cloud fraction threshold. The satellite and model SIF (climatology and anomalies) are generally comparable, although there are some differences in the spatio-temporal distributions. Overall, the model is shown to produce a reasonable response of SIF to the drought/heat wave. At the same time, it provides insight into how the different components of SIF and SIF itself may respond to heat and water stress. Note that the model data are output as monthly means (averages of daily means) and so cannot be directly compared with instantaneous satellite SIF measurements taken at a specific time of day.

3.3 Inter-annual variations in SIF and NDVI

Figure 10 compares interannual variability (2007-2013) of the GOME-2 SIF and the GIMMS NDVI integrated over April-September for the six boxes examined above. Note that the axes are normalized to the maximum values. For all boxes except box 3, SIF and NDVI are correlated (r^2 values of 0.75−0.91). This relatively high correlation confirms that fPAR is a major contributor to the interannual variability of SIF in this region.

An interesting feature is the deviation of the fitted slopes (solid lines) from the one-to-one (1:1) lines (dashed). For example, for box 4 (primarily grasslands), the minimum value of SIF in 2010 is > 60% less than the maximum, while that of NDVI is ~35% less than maximum. While fPAR impacts both SIF and NDVI, SIF is additionally affected by fluorescence efficiency, related to photosynthesis and light-use efficiency. This may explain the larger percentage drought impact on SIF as compared with NDVI for these boxes. It should also be noted that fPAR is somewhat non-linear with respect to NDVI (*e.g.,* Los *et al.,* 2000).

4. Conclusions

We have examined the response of canopy-level SIF to heat and drought stress in 2010 over a portion of Russia that includes both agricultural areas and forested regions using satellite SIF and NDVI observations as well as model simulations. SIF and NDVI satellite data show similar signs of drought stress early in the growing season well before the onset of the heat wave both inside and outside the main area of the heat wave. Large declines in 2010 are seen in both quantities throughout much of the drought-affected area. Areas dominated by crops and grasslands showed significant drops in SIF and NDVI, while regions of predominantly mixed forest showed small to insignificant reductions.

We simulated SIF using a global land surface model forced by observations-based meteorological fields. The model simulated large negative anomalies in 2010 SIF similar to those seen in the GOME-2 satellite SIF data. The model also produced spatial and temporal patterns of the SIF anomalies similar to those derived from GOME-2, although with some exceptions. There exists potential to improve the model's response by using the satellite SIF observations for data assimilation (modification of the model's prognostic variables) and/or parameter estimation; this could be a topic of a future study. Although the model simulated earlier drought-related declines in photosynthesis as compared with fPAR, the NDVI data suggest that there were significant declines in fPAR early in the growing season for areas dominated by crops and grasslands.

New satellite sensors, such as the recently launched Orbiting Carbon Observatory 2 (OCO-2) (Frankenberg *et al*., 2014) and the TROPOspheric Monitoring Instrument (TROPOMI) (Veefkind *et al*., 2012) to be launched in 2016 will offer higher spatial resolution measurements as compared with GOME-2. In addition, these satellites will make measurements from sun-synchronous polar orbits with local overpass times in the early afternoon, when stress effects should be peaking and may be larger during the morning overpass of GOME-2. We plan to utilize these new data sets for further examination of the manifestation of stress effects on observed SIF. We also plan further comparisons between satellite and modeled SIF with an aim towards using the satellite SIF data to improve models as demonstrated by the pioneering study of Zhang *et al*. (2014).

Appendix

Here, we compare seasonal cycle of NDVI from GIMMS, MAIAC, and the standard Aqua MODIS product MYD13Q1, 16-day L3 global 250m SIN grid collection 5 (MYD13) for the climatology and 2010. The products differ mainly in how the cloud detection is applied. The MYD13 data have been additionally filtered for cloud and aerosol contamination following the methodology of Xu *et al*. (2011). All three NDVI data sets look similar, although there are a few exceptions. For example, in box 1, the climatologies from GIMMS and MAIAC are similar, but MYD13 shows a significantly lower peak than the other two. Also, climatological MYD13 in box 4 does not show a dip in middle June as the GIMMS and MAIAC do. For other boxes, the seasonal cycles for all three products are more similar.

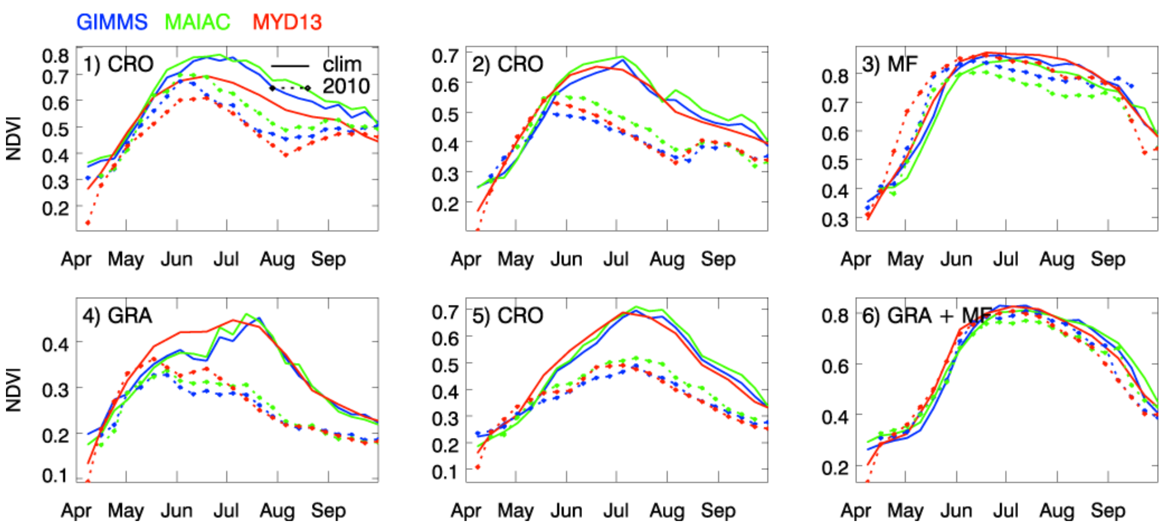

Figure A1: Seasonal cycles of NDVI from GIMMS (blue), MAIAC (green) and standard product of MYD13Q1 (red); solid lines (broken lines with symbols) are for the climatology, (2010). Averages are computed using data only where all three data sets provided successful retrievals. MYD13 data are interpolated to match 8-day intervals of the other data sets.

Acknowledgement

The authors gratefully acknowledge the EUMETSAT, GMAO, and MODIS data processing and algorithm development teams for making available the GOME-2 level 1b,

GEOS-5 MERRA, and MODIS level 2 data sets, respectively, used here.

References

Berry, J., Frankenberg, C., Wennberg, P., Baker, I., Bowman, K., Castro-Contreas, S., *et al*. (2013). New methods for measurements of photosynthesis from space. Presented at the 2013 NASA terrestrial ecology science team meeting, La Jolla, CA, April 30-May 2, 2013, http://www.kiss.caltech.edu/workshops/photosynthesis2012/NewMethod2.pdf.

Damm, A., Elbers, J., Erler, A., Giolis, B., Hamdi, K., Hutjes, R.W.A., *et al*. (2010). Remote sensing of sun-induced fluorescence to improve modeling of diurnal courses of gross primary production (GPP), *Global Change Biology, 16,* 171-186.

Daumard, F., Champagne, S., Fournier, A., Goulas, Y., Ounis, A., Hanocq, J.-F., & Moya, I. (2010). A field platform for continuous measurement of canopy fluorescence. *IEEE Transactions on Geoscience and Remote Sensing, 48,* 3358-3368.

Frankenberg, C., Fisher, J., B., Worden, J. *et al*. (2011). New global observations of the terrestrial carbon cycle from GOSAT: patterns of plant fluorescence with gross primary productvity. *Geophysical Research Letters, 38,* L17706, doi:10.1029/2011GL048738.

Frankenberg, C., O'Dell, C., Guanter, L., & McDuffie, J. (2012). Remote sensing of near-infrared chlorophyll fluorescence from space in scattering atmospheres: implications for its retrieval and interferences with atmospheric CO_2 retrievals. *Atmospheric Measurement Techniques, 5*, 2081--2094, doi:10.5194/amt-5-2081-2012.

Frankenberg, C., O'Dell, C., Berry, J., Guanter, L., Joiner, J., Köhler, P., Pollack, R., & Taylor, T. E. (2014). Prospects for chlorophyll fluorescence remote sensing from the Orbiting Carbon Observatory-2. *Remote Sensing of Environment, 147*, 1-12.

Friedl, M.A., Sulla-Menashe, D., Tan, B., Schneider, A., Ramankutty, N., Sibley, A., & Huang, X. (2010). MODIS Collection 5 global land cover: Algorithm refinements and characterization of new datasets. Remote Sensing of Environment, *114*, 168–182.

Grumm, R. H. (2011). The central European and Russian heat event of July-August 2010. *Bulletin of the American Meteorological Society, 92*, 1285-1296.

Guanter, L., Zhang, Y., Jung, M., Joiner, J., Voigt, M., Berry, J. A., Frankenberg, C., Huete, A. R., Zarco-Tejada, P., Lee, J.-E., Moran, M. S., Ponce-Campos, G., Beer, C., Camps-Valls, G., Buchmann, N., Gianelle, D., Klumpp, K., Cescatti, A., Baker, J. M., & T. J. Griffis (2014). Global and time-resolved monitoring of crop photosynthesis with chlorophyll fluorescence. *Proceeding of the National Academy of Sciences,* doi: 10.1073/pnas.1320008111.

Guanter, L., Alonso, L., Gómez-Chova, L., Amorós-López, L., Vila-Francés, J., & Moreno, J. (2007). Estimation of solar-induced vegetation fluorescence from space measurements. *Geophysical Research Letters, 34*, doi:10.1029/2007GL029289.

Guanter, L., Frankenberg, C., Dudhia, A., Lewis, P. E., Gomez-Dans, J., Kuze, A., Suto,

H. & Grainger, R. G. (2012). Retrieval and global assessment of terrestrial chlorophyll fluorescence from GOSAT space measurements. *Remote Sensing of Environment, 121,* 236-251.

Huete, A. R., Didan, K., Miura, T., Rodriguez, E. P., Gao, X., & Ferreira, L. G. (2002). Overview of the radiometric and biophysical performance of the MODIS vegetation indices. *Remote Sensing of Environment, 83,* 195-213.

Joiner, J., Yoshida, Y., Vasilkov, A. P., Schaefer, K., Jung., M., Guanter, L., Zhang, Y., Garrity, S., Middleton, E. M., Huemmrich, K. F., Gu, L., & Marchesini, L. B. (2014). The seasonal cycle of satellite chlorophyll fluorescence observations and its relationship to vegetation phenology and ecosystem-atmosphere carbon exchange. *Remote Sensing of Environment, 152*, 375-391, doi:10.1016/j.rse.2014.06.022

Joiner, J., Guanter, L., Lindstrot, R., Voigt, M., Vasilkov, A. P., Middleton, E. M., Huemmrich, K. F., Yoshida, Y., & Frankenberg, C. (2013). Improved global monitoring of terrestrial chlorophyll fluorescence from moderate spectral resolution near-infrared satellite measurements: Methodology, simulations, and application to GOME-2. *Atmospheric Measurement Techniques, 6*, 2803-2823, doi:10.5194/amt-6-2803-2013.

Joiner, J., Yoshida, Y., Vasilkov, A. P., Middleton, E. M., Campbell, P. K. E., Yoshida, Y., Kuze, A., & Corp, L. A. (2012). Filling-in of near-infrared solar lines by terrestrial fluorescence and other geophysical effects: simulations and space-based observations from SCIAMACHY and GOSAT. *Atmospheric Measurement Techniques*, *5*, 809-829, doi:10.5194/amt-5-809-2012.

Joiner, J., Yoshida, Y., Vasilkov, A. P., Yoshida, Y., Corp, L. A., & Middleton, E. M. (2011). First observations of global and seasonal terrestrial chlorophyll fluorescence from space. *Biogeosciences*, *8*, 637-651, doi:10.5194/bg-8-637-2011.

Köhler, P., Guanter, L., & Joiner, J. (2014). A linear method for the retrieval of sun-induced chlorophyll fluorescence from GOME-2 and SCIAMACHY data. *Atmos. Meas. Tech. Discuss., 7*, 12173-12217, doi:10.5194/amtd-7-12173-2014.

Koster, R. D., M. J. Suarez, A. Ducharne, M. Stieglitz, and P. Kumar, (2000). A catchment-based approach to modeling land surface processes in a general circulation model: 1. Modelstructure. *J. Geophys. Res., 105,* 24 809–24 822, doi:10.1029/2000JD900327.

Koster, R. D., G. K. Walker, G. J. Collatz, and P. E. Thornton (2014). Hydroclimatic controls on the means and variability of vegetation phenology and carbon uptake. *J. Climate, 27,* 5632-5652.

Lee, J.-E., Berry, J., van der Tol, C., Guanter, L., Damm, A., Baker, I., & Frankenberg,

C. (2014). Calculations for chlorophyll fluorescence incorporated into the Community Land Model version 4. *Global Change Biology*, under revision.

Lee, E., Felzer, B. S., & Kothavala, Z. (2013). Effects of nitrogen limitation on hydrological processes in CLM4-CN. *Journal of Advances in Modeling Earth Systems, 5,* doi:10.1002/jame.20046.

Lee, J.-E., Frankenberg, C., van der Tol, C., Berry, J. A., Guanter, L., Boyce, C. K., Fisher, J. B., Morrow, E., Worden, J. R., Asefi, S., Badgley, G., & Saatchi, S. (2013). Forest productivity and seasonal water stress in Amazonia: observations from GOSAT chlorophyll fluorescence. *Proceedings of the Royal Society B: Biological Sciences, 280,* 20130171, http://dx.doi.org/10.1098/rspb.2013.0171.

Los, S. O., Pollack, N. H., Parris, M. T., Collatz, G. J., Tucker, C. J., Sellers, P. J., Malmström, C. M., DeFries, R. S., Bounoua, L. & Dazlich, D. A. (2000). A global 9-yr biophysical land surface dataset from NOAA AVHRR data. *Journal of Hydrometeorolgy*, *1,* 183–199, doi:10.1175/1525-7541.

Louis, J., Ounis, A., Ducruet, J.-M., Evain, S., Laurila, T., Thum, T., *et al*. (2005). Remote sensing of sunlight-induced chlorophyll fluorescence and reflectance of Scots pine in the boreal forest during spring recovery, *Remote Sensing of Environment, 96,* 37-48.

Lyapustin A., Martonchik J., Wang Y., Laszlo I., & Korkin S. (2011a). Multiangle implementation of atmospheric correction (MAIAC): 1. Radiative transfer basis and look-up tables. *Journal of Geophysical Research*, *116*, D03210.

Lyapustin, A., Wang, Y., Laszlo, I., Kahn, R., Korkin, S., Remer, L., & Reid, J. S. (2011b). Multiangle implementation of atmospheric correction (MAIAC): 2. Aerosol algorithm. *Journal of Geophysical Research, 116*, D03211.

Meroni, M., Picchi, V., Rossini, M., Cogliati, S., Panigada, C., Nali, C., Lorenzini, G., & Colombo, R. (2008). Leaf level early assessment of ozone injuries by passive fluorescence and photochemical reflectance index. *International Journal of Remote Sensing, 29*, 5409-5422, 2008.

Middleton, E. M., Huemmrich, K. F., Cheng, Y.-B., & Margolis, H. A. (2011). Spectral bio-indicators of photosynthetic efficiency and vegetation stress. In: Hyperspectral Remote Sensing of Vegetation, edited by: Thenkbail, P. S., Lyon, J. G., Huete, A., Taylor & Francis, Cat. # K12019, 2011.

Middleton, E. M., Cheng, Y.-B., Corp, L. A., Huemmrich, K. F., Campbell, P. K. E., Zhang, Q.-Y., Kustas, W. P., & Russ, A. L. (2009). Diurnal and seasonal dynamics of canopy-level solar-induced chlorophyll fluorescence and spectral reflectance indices in a cornfield. Proc. 6th EARSeL SIG Workshop on Imaging Spectroscopy, CD-Rom, 12 pp., Tel-Aviv, Israel, 16-19 March 2009.

Monteith, J. L. (1972). Solar radiation and productivity in tropical ecosystems. *Journal of Applied Ecology, 9*, 747-766.

Munro, R., Eisinger, M., Anderson, C., Callies, J., Corpaccioli, E., Lang, R., Lefebvre, A., Livschitz, Y., & Perez Albinana, A. (2006). GOME-2 on MetOp, from In-Orbit Verification to Routine Operations. In: *Proceedings of EUMETSAT Meteorological Satellite Conference*, Helsinki, Finland, 12-16 June 2006.

Myneni, R. B., Hall, F. G., Sellers, P. J., & A. L. Marshak (1995). The interpretation of spectral vegetation indexes. *IEEE Transactions on Geoscience and Remote Sensing, 33*, 481-486.

Myneni, R. B., Ramakrishna, R., Nemani, R. R., & Running, S. W. (1997). Estimation of global leaf area index and absorbed PAR using radiative transfer models. *IEEE Transactions on Geoscience and Remote Sensing, 3,* 1380–1393.

Oleson, K. W., Lawrence, D. M., Bonan, G. B., Flanner, M. G., Kluzek, E., Lawrence, P. J., *et al*. (2010). Technical description of version 4.0 of the Community Land Model (CLM). NCAR Tech. Note NCAR/TN-4781STR, 257 pp.

Parazoo, N. C., Bowman, K., Frankenberg, C., Lee, J. -E., Fisher, J. B., Worden, J. *et al*. (2013). Interpreting seasonal changes in the carbon balance of southern Amazonia using measurements of XCO_2 and chlorophyll fluorescence from GOSAT. *Geophysical Research Letters*, *40*, 2829–2833.

Porcar-Castell, A., Tyystjärvi, E., Atherton, J., van der Tol, C., Flexas, J., Pfündel, E. E., Moreno, J., Frankenberg, C., and Berry, J. A. (2014). Linking chlorophyll *a* fluorescence to photosynthesis remote sensing application: mechanisms and challenges. *Journal of Experimental Botany, 65*, 4065-4095, doi:10.1093/jxb/eru191.

Randerson, J. T., Thompson, M. V., Conway, T. J., Fung, I. Y., & Field, C. B. (1997). The contribution of terrestrial sources and sinks to trends in the seasonal cycle of atmospheric carbon dioxide. *Global Biogeochemical Cycles, 11*, 535-560.

Reichle, R. H., Koster, R. D., De Lannoy, G. J. M., Forman, B. A., Liu, Q., Mahanama, S. P. P., & Toure, A. (2011). Assessment and enhancement of MERRA land surface hydrology estimates. *Journal of Climate*, *24*, 6322-6338, doi:10.1175/JCLI-D-10-05033.1.

Running, S. W., Nemani, R. R., Heinsch, F. A., Zhao, M., Reeves, M., & Hashimoto, H. (2004). A continuous satellite-derived measure of global terrestrial primary production. *Bio-Science, 54*, 547–560.

Rienecker, M. M., M.J. Suarez, R. Gelaro, R. Todling, J. Bacmeister, E. Liu, M.G. Bosilovich, S.D. Schubert, L. Takacs, G.-K. Kim, S. Bloom, J. Chen, D. Collins, A. Conaty, A. da Silva, *et al*. (2011). MERRA: NASA's modern era retrospective-analysis for research and applications. *Journal of Climate, 24*, 3624-3648, doi: 10.1175/JDLI-D-11_00015.1.

Thornton, P. E., Doney, S. C., Lindsay, K., Moore, J. K., Mahowald, N., Randerson, J. T., Fung, I., Lamarque, J. -F., Feddema, J. J., & Lee, Y. -H. (2009). Carbon-nitrogen interactions regulate climate-carbon cycle feedbacks: Results from an atmosphere-ocean general circulation model. *Biogeosciences, 6,* 2099–2120, doi:10.5194/bg-6-2099-2009.

Tucker, C. J. (1979). Red and photographic infrared linear combinations for monitoring vegetation. *Remote Sensing of Environment, 8*, 127-150.

Tucker, C.J., Holben, B. N., Elgin J. H., & McMurtrey, J. E. (1981). Remote sensing of total dry-matter accumulation in winter wheat. *Remote Sensing of Environment 11*:171-189.

Tucker, C. J. & Sellers, P. J. (1986). Satellite remote-sensing of primary production. *International Journal of Remote Sensing, 7*, 1395–1416.

Tucker, C. J., Pinzon, J. E. , Brown, M. E. , Slayback, D. A. , Pak, E. W. , Mahoney, R. , Vermote, E. F. , & Saleous, N. E. (2005). An Extended AVHRR 8-km NDVI Dataset Compatible with MODIS and SPOT Vegetation NDVI Data. *International Journal of Remote Sensing, 26*, 4485–4498.

Van der Tol, C., Berry, J. A., Campbell, P. K. E., & Rascher, U. (2014). Models of fluorescence and photosynthesis for interpreting measurements of solar induced chlorophyll fluroescence. *Journal of Geophysical Research,* doi: 10.1002/2014JG002713.

Veefkind, J. P., Aben, I., McMullan, K., Forster, H., de Vries, J., Otter, G., Claas, J., *et al*. (2012). TROPOMI on the ESA Sentinel-5 Precursor: a GMES mission for global observations of the atmospheric composition for climate, air quality and ozone layer applications. *Remote Sensing of Environment, 120,* 70-83, doi: 10.1016/j.rse.2011.09.027.

Xu, L., Samanta, A., Costa, M. H., Ganguly, S., Nemani, R. R., & Myneni, R. B. (2011). Widespread decline in greenness of Amazonian vegetation due to the 2010 drought, *Geophys. Res. Lett., 38*, L07402, doi:10.1029/2011GL046824.

Zhang, Y., Guanter, L., Berry, J. A., Joiner, J., van der Tol, C., Huete, A., Gitelson, A., Voigt, M., & Koehler, P. (2014). Estimation of vegetation photosynthetic capacity from space-based measurements of chlorophyll fluorescence for terrestrial biosphere models. *Global Change Biology,* doi:10.1111/gcb.12664.

Table 1: Location of the twelve box regions (center of 2° longitude × 1° latitude box) and major IGBP vegetation types; CRO: croplands, GRA: grasslands, MF: mixed forest. The percentage of the coverage is also shown (not shown if the coverage < 5%).

Box number	Latitude	Longitude	Vegetation cover (%)
1	54.5° N	48.0° E	CRO: 62 GRA + MF: 14 MF: 11
2	52.5° N	55.0° E	CRO: 97
3	54.5° N	57.7° E	MF: 95 GRA + MF: 5
4	51.0° N	67.5° E	GRA: 100
5	54.0° N	67.5° E	CRO: 81 GRA: 10 GRA + MF: 8
6	56.5° N	70.5° E	GRA + MF: 86 MF: 8 CRO: 4

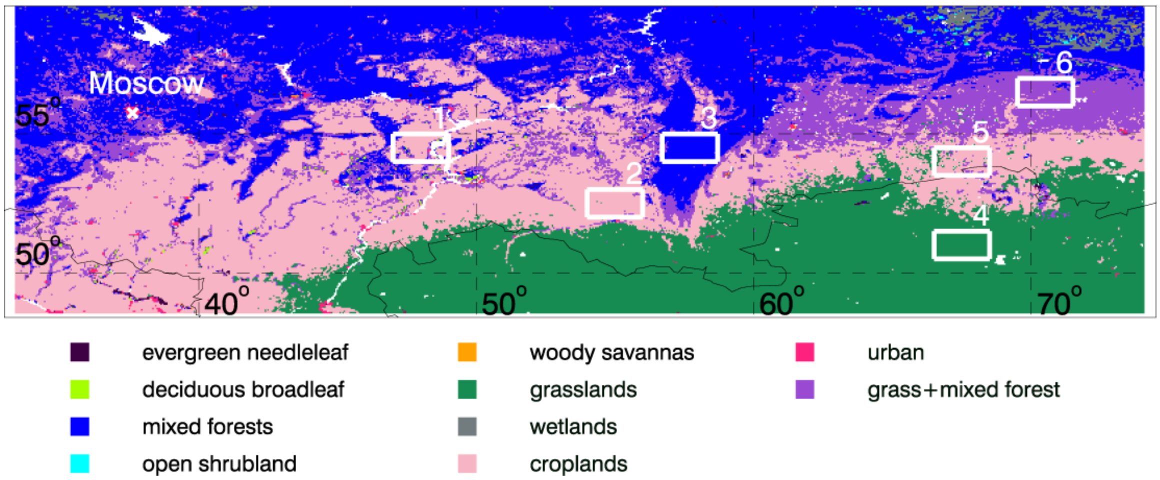

Figure 1: Map of land cover type for 2010. The six box regions used for further analysis are also shown.

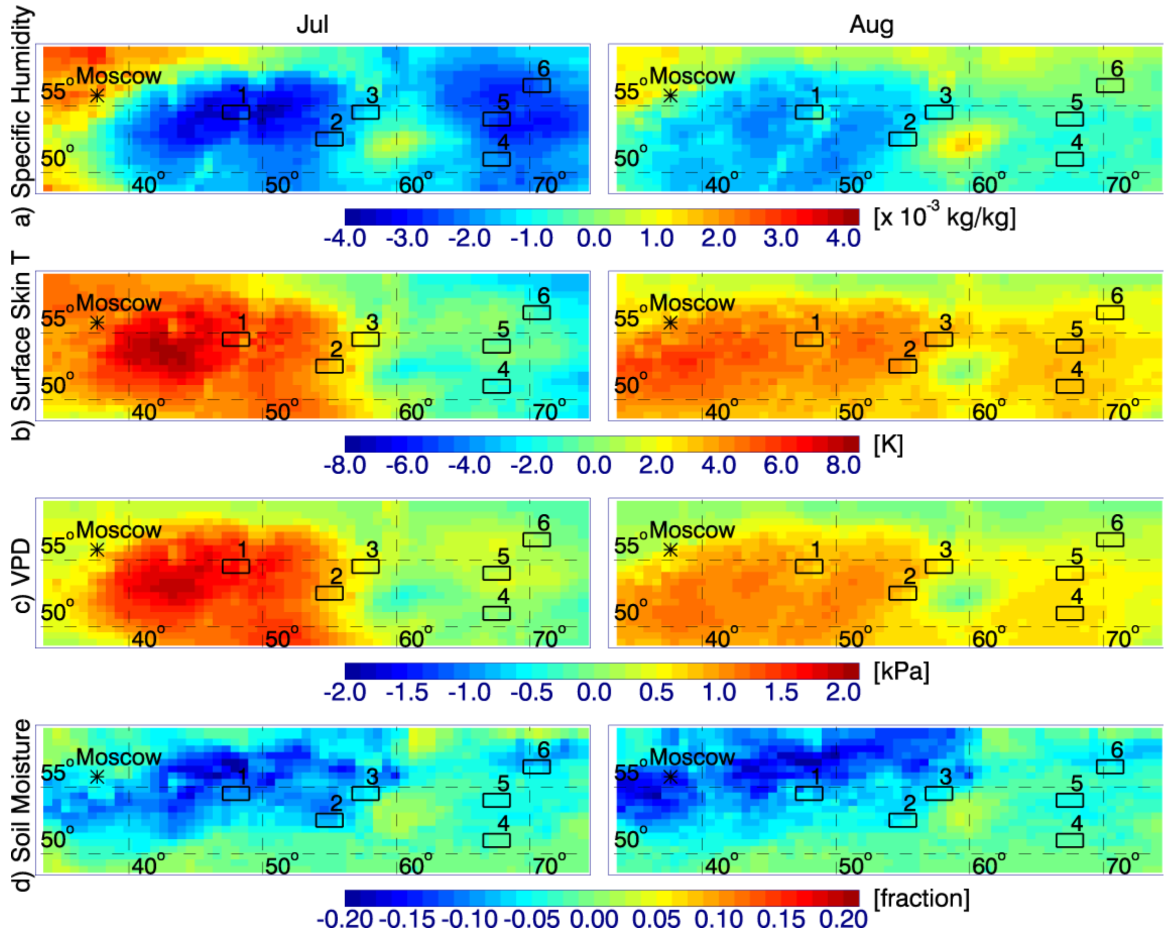

Figure 2: Maps of July (left column) and August (right) 2010 anomalies of MERRA meteorological fields (differences between July (August) 2010 and average of all other July's (August's) from 2007-2013 not including 2010): a) specific humidity (anomalies in terms of %), b) surface skin temperature (anomalies in K), and c) vapor pressure deficit (anomalies in terms of kPa).

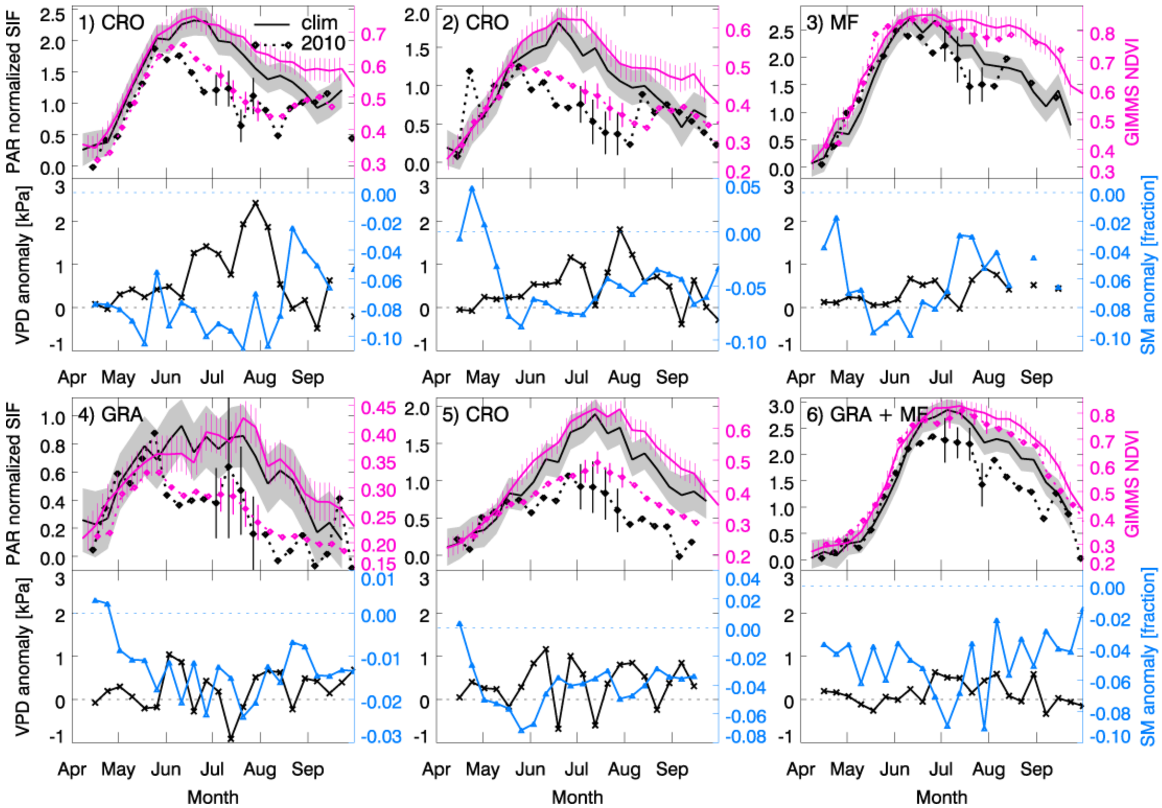

Figure 3: Top panels: Seasonal cycle (8-day means) of GOME-2 fluorescence [mW/m^2/nm/sr] (black lines), Aqua MODIS GIMMS NDVI [unitless] (magenta lines); solid lines (broken lines with symbols) are for climatology (2010). Error ranges are indicated as shading or vertical bars where for clarity only a few representative error bars are shown (in July) for the 2010 data. Bottom panels: Vapor pressure deficit anomaly [hPa] (black line) and soil moisture (SM) anomaly [fraction] (blue line) for the six boxes shown in Fig. 1. Anomalies are calculated as 2010 - climatology.

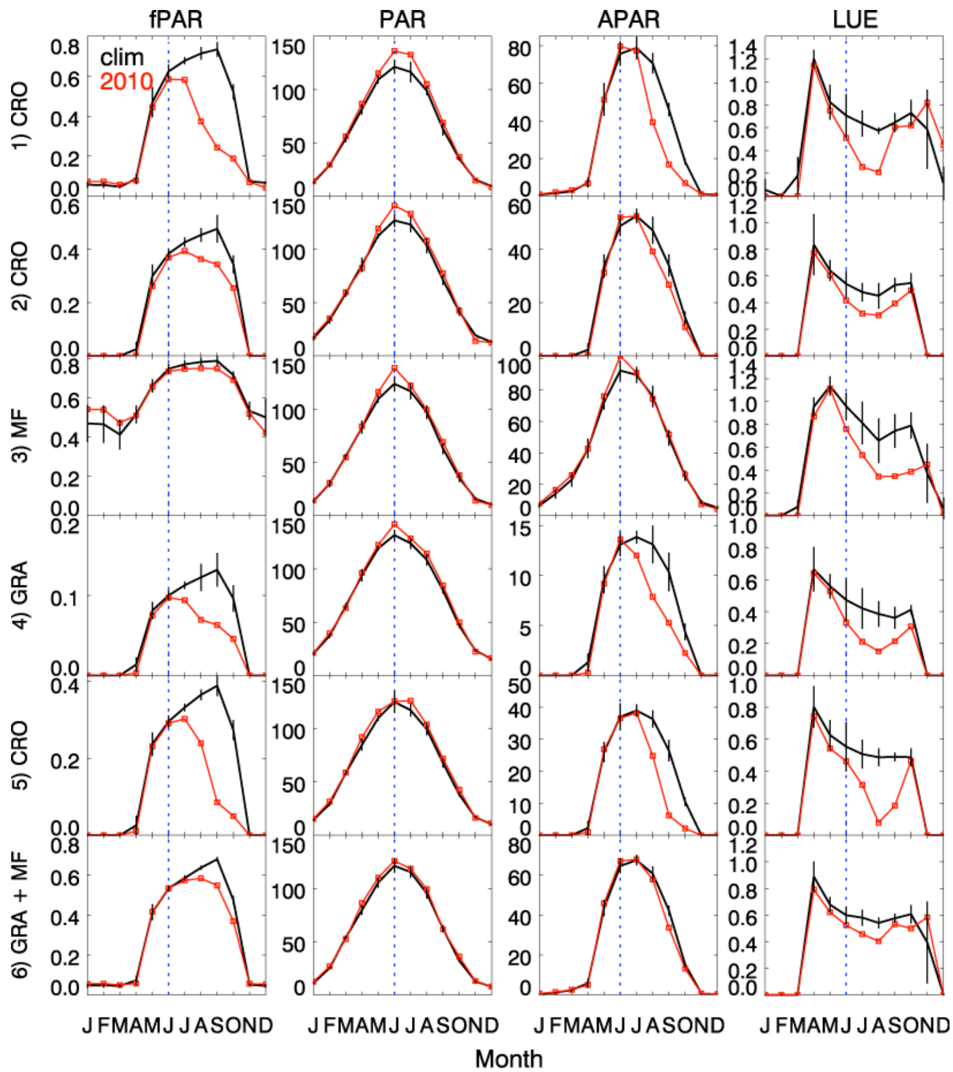

Figure 4: Monthly mean Catchment-CN land surface model results with MERRA forcing for selected boxes shown in Fig. 1. Black (red) lines represent climatological mean values (2010 values). From left column, fPAR [unitless], PAR [W/m^2], APAR [W/m^2] and d) LUE [μg C/J]. LUE is calculated as GPP/APAR. The black vertical bars indicate standard deviations. The blue vertical dotted lines indicate June. Note: different y-scales are used for the different boxes.

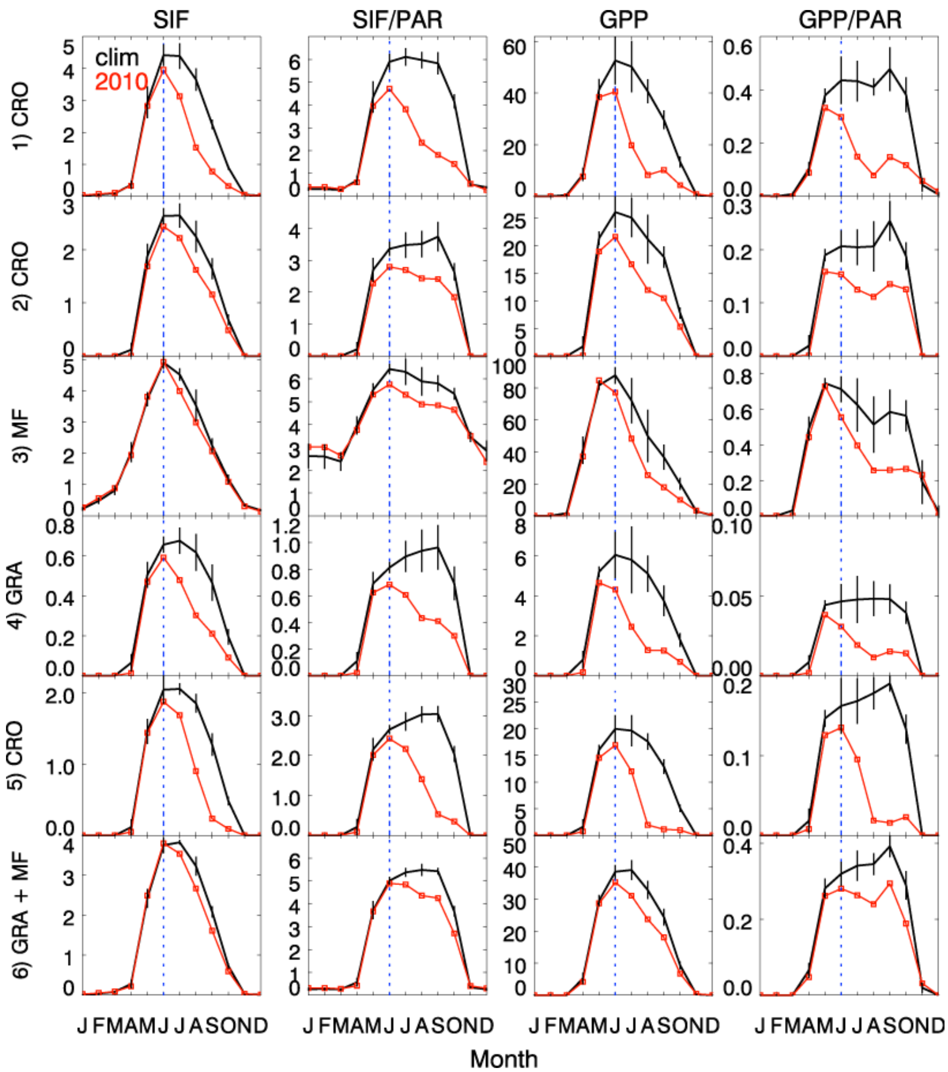

Figure 5: The same as Fig.4 but for (from left) SIF [μmol photons/m^2/s], SIF normalized with respect to PAR [× 10^{-3}], GPP [μg C/m^2/s] and GPP normalized with respect to PAR [μg C·W/s].

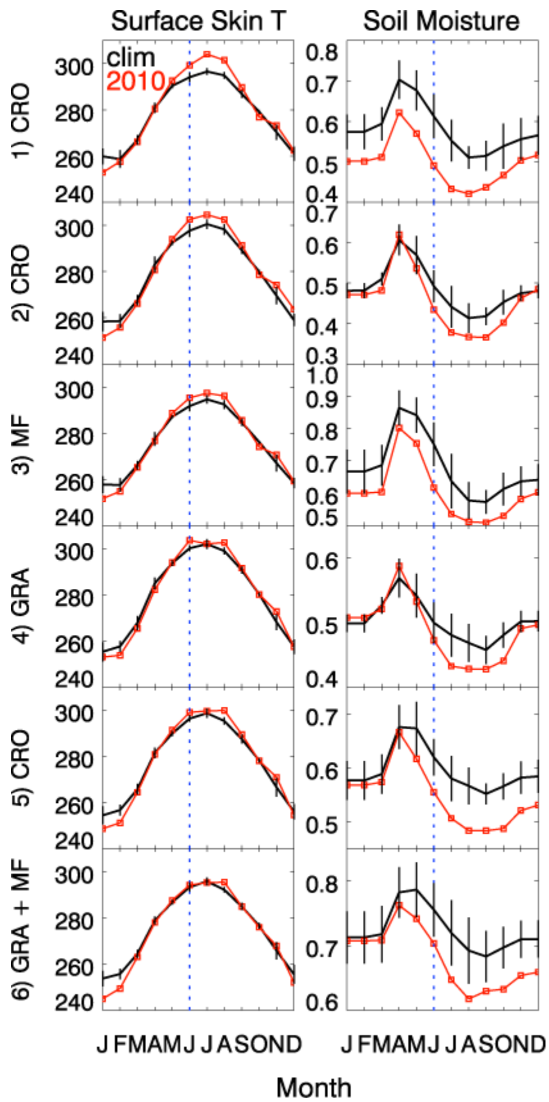

Figure 6: Same as Fig. 4 but for surface skin temperature [K] (left) and root-zone soil moisture [fraction] (right).

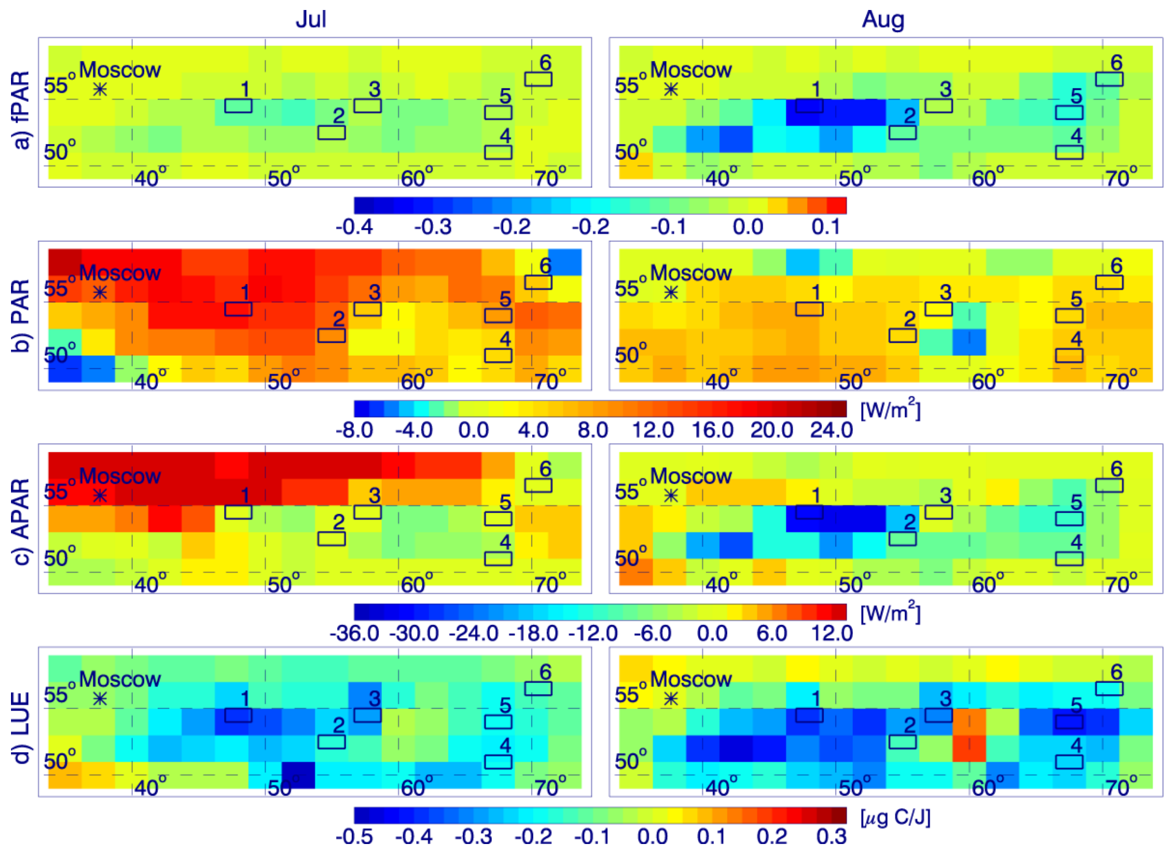

Figure 7: Maps of 2010 anomalies for July (right column) and August (left), computed as differences between July (August) 2010 and average of all other July's (August's) from 2007-2013 not including 2010 calculated using MERRA-forced land surface model simulations: a) fPAR [unitless], b) PAR [W/m^2], c) APAR [W/m^2] and d) LUE [µg C/J].

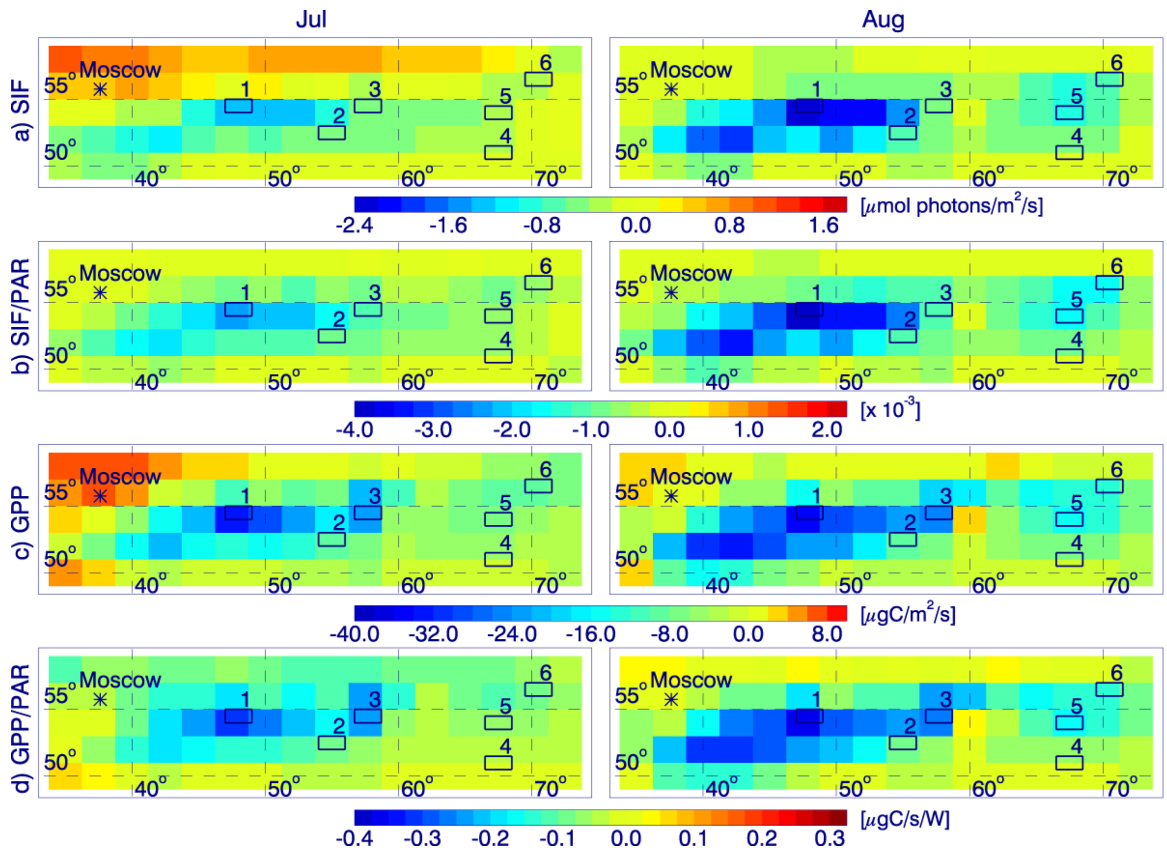

Figure 8: Same as Fig.7 but for: a) SIF [μmol photons/m^2/s], b) SIF normalized with respect to PAR [× 10^{-3}], c) GPP [μg C/m^2/s], and d) GPP normalized with respect to PAR [μg C/s/W].

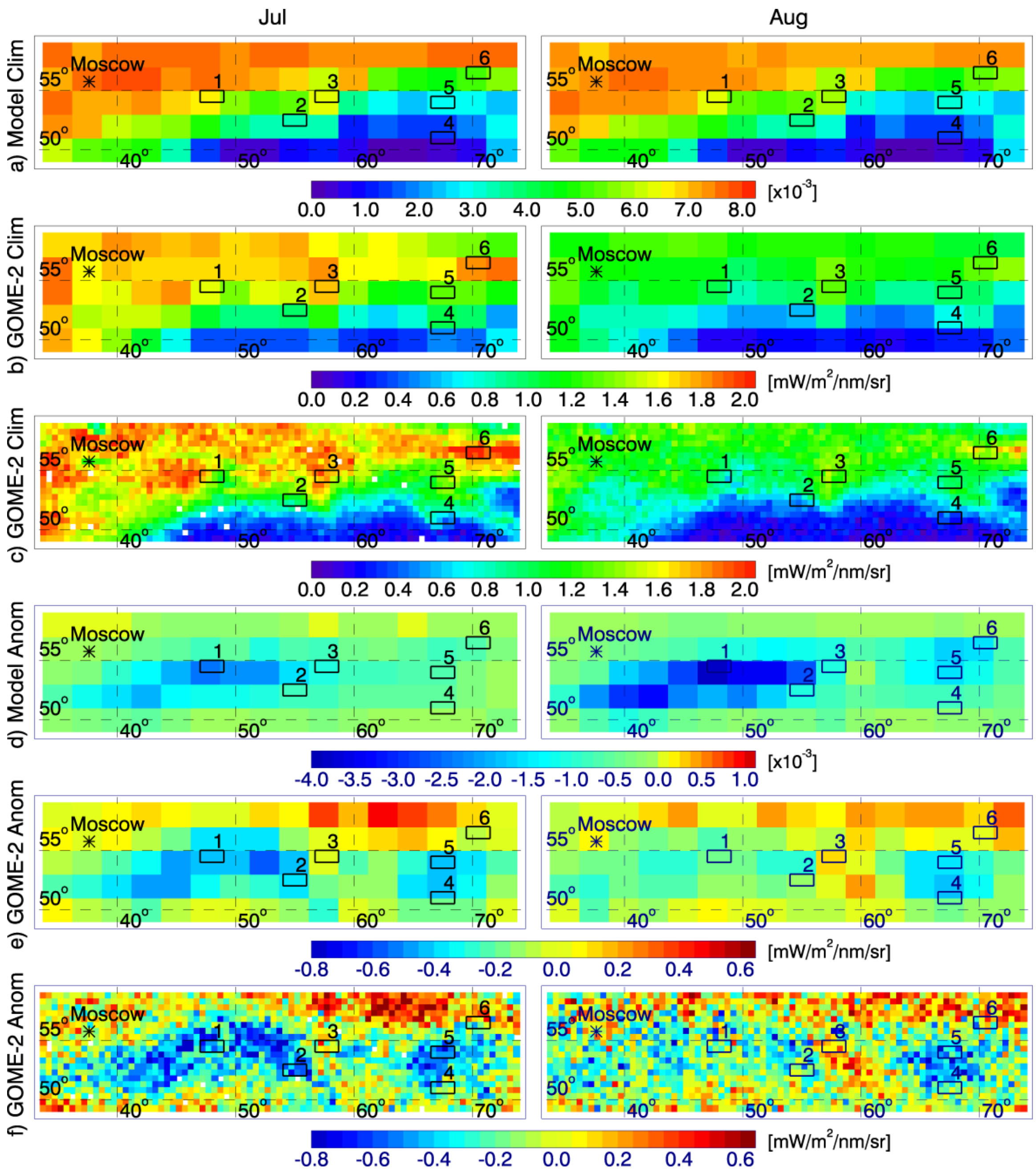

Figure 9: Maps of the SIF monthly climatology (a, b and c) and anomaly (d, e and f) for July (left column) and August (right) from MERRA-forced land surface model simulations (a and d), GOME-2 with 2.0°×2.5° resolutions (b and e), and GOME-2 with 0.5°×0.5° resolutions (c and f). Anomalies are computed as in Fig. 3. Model SIF is normalized with respect to model PAR.

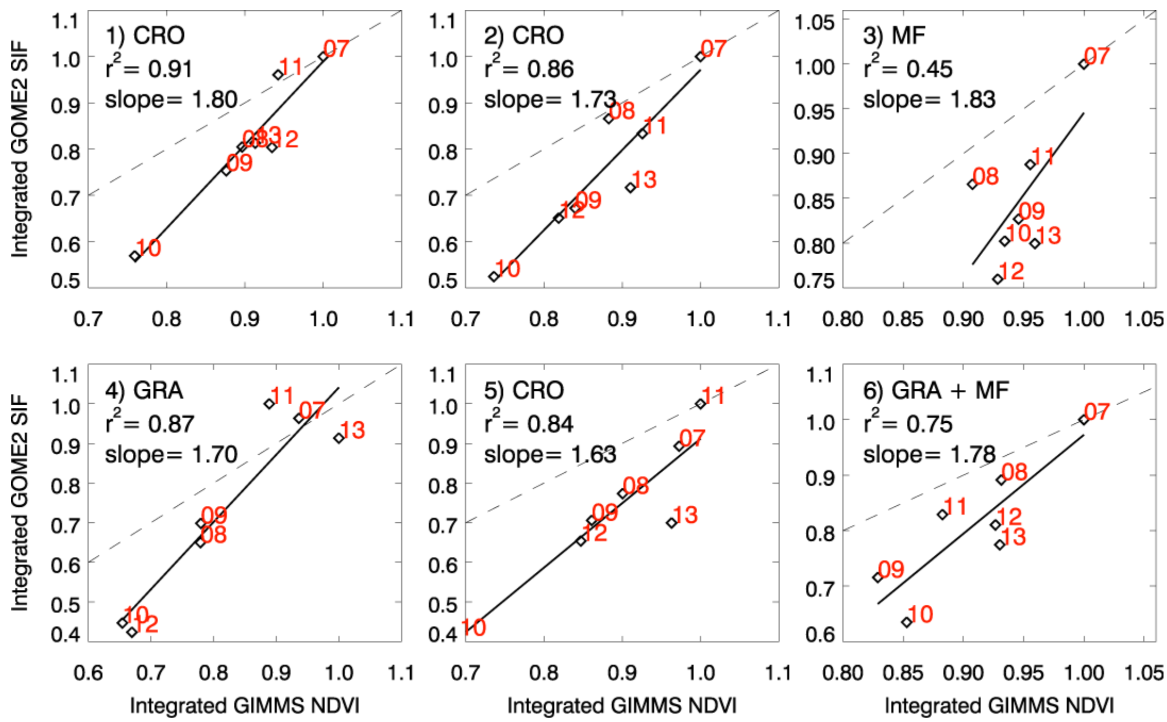

Figure 10: Scatter diagram of April-September integrated GOME-2 SIF and Aqua MODIS GIMMS NDVI for each year in the range 2007 to 2013 for the six boxes shown in Fig. 1; red numbers indicate years (i.e., 07=2007). Values are scaled (divided by the maximum for each box). Solid line: linear fit; dashed: 1:1 line. The dominant vegetation type, correlation (r^2), and slope values are provided for each box.